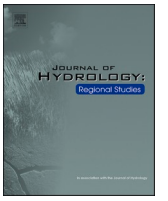
Journal of Hydrology: Regional Studies 68 (2026) 104001



Contents lists available at ScienceDirect

Journal of Hydrology: Regional Studies

journal homepage: www.elsevier.com/locate/ejrh



Impacts of climate and land use changes on water retention in the transboundary Yuanjiang-Red River Basin: Historical attribution and future projections

Yi Zou [a,b], Roberto Ranzi [b], Xuan Ji [a], Paolo Colosio [b], Nguyen Hao Quang [c,d], Xuan Luo [a], Fan Zhou [a], Jianxing Li [a], Yungang Li [a,e,*]

[a] Institute of International Rivers and Eco-security, Yunnan Key Laboratory of International Rivers and Transboundary Eco-security, Yunnan University, Kunming, 650504, China
[b] Department of Civil, Environmental, Architectural Engineering and Mathematics, Università degli Studi di Brescia, Via Branze, 43, Brescia, 25123, Italy
[c] Laboratory of Environmental Sciences and Climate Change, Institute for Computational Science and Artificial Intelligence, Van Lang University, Ho Chi Minh City, 70000, Viet Nam
[d] Faculty of Environment, Van Lang School of Technology, Van Lang University, Ho Chi Minh City, 70000, Viet Nam
[e] Ministry of Education Key Laboratory for Transboundary Eco-security of Southwest China, Yunnan University, Kunming, 650504, China

ARTICLE INFO

Keywords:
Water retention
Transboundary basin
Climate change
Land-use change
Bayesian model averaging
EOF
Spatial heterogeneity

ABSTRACT

Study region: the Yuanjiang–Red River Basin (YRRB), Southeast Asia.
Study focus: Water retention (*WR*) capacity in the transboundary YRRB has been increasingly affected by combined climate and land-use changes. However, limited quantitative attribution of historical drivers and uncertain future projections hinder the development of effective cross-border adaptation strategies. This study integrated the Variable Infiltration Capacity model, a fixed-varying scenario design, and variable-specific Bayesian model averaging of bias-corrected, downscaled Coupled Model Intercomparison Project Phase 6 climate projections to attribute historical *WR* changes during 1973–2015 and project *WR* changes during 2016–2050 under three Shared Socioeconomic Pathway scenarios.
New hydrological insights for the region: Historical *WR* averaged 572 mm and showed a nonsignificant decline of 18 mm decade^{-1} , primarily attributable to climate change. Local buffering effects associated with land-use change were insufficient to offset this basin-wide decline. Future *WR* is projected to decline by 29.6%–33.5%. Empirical orthogonal function (EOF) analysis indicated a shift toward greater spatial heterogeneity. Relative to SSP126, EOF1 decreased from 79% to 64%–68%, whereas EOF2 increased from 7% to 12%–17% under SSP245 and SSP585. This overall shift was associated with the combined effects of declining precipitation and increasing evapotranspiration. These findings inform coordinated cross-border ecological restoration and spatially targeted water management between China and Vietnam.

* Corresponding author at: Institute of International Rivers and Eco-security, Yunnan Key Laboratory of International Rivers and Transboundary Eco-security, Yunnan University, Kunming 650504, China.
E-mail address: ygli@ynu.edu.cn (Y. Li).

https://doi.org/10.1016/j.ejrh.2026.104001
Received 18 June 2026; Received in revised form 11 August 2026; Accepted 17 September 2026
Available online 21 September 2026
2214-5818/© 2026 The Author(s). Published by Elsevier B.V. This is an open access article under the CC BY-NC-ND license (http://creativecommons.org/licenses/by-nc-nd/4.0/).

1. Introduction

Water scarcity is becoming increasingly severe and may hinder the achievement of multiple Sustainable Development Goals (SDGs) through direct or indirect pathways (She et al., 2024). Climate change increasingly threatens water security, while human activities such as land-use change alter watershed hydrological processes (Ranzi et al., 2012; IPCC, 2023; Xiao et al., 2023). Water retention (*WR*) refers to the process and ability of ecosystems to intercept, infiltrate, store, and regulate precipitation through the canopy layer, litter layer, soil layer, and other water bodies within a given spatial and temporal domain (Šatalová and Kenderessy, 2017; Zhao et al., 2024; Xu et al., 2025). By moderating surface runoff and promoting groundwater recharge, *WR* contributes to river-flow regulation and represents a fundamental ecosystem service closely linked to hydrological processes, vegetation, and soil nutrient cycling (Wu et al., 2023).

Climate change and human activities are the two primary drivers influencing watershed *WR* capacity. Climate change primarily affects the basin water cycle and surface conditions by elevating temperatures and altering spatiotemporal precipitation patterns, thereby introducing additional constraints and uncertainties to projected *WR* dynamics (Wang et al., 2022; Wang et al., 2025). Human activities affect runoff generation, flow routing, and sediment transport through land-use/land-cover change and reservoir regulation (Ranzi et al., 2012; Xiao et al., 2023). Together, these drivers reshape key hydrological processes and *WR* capacity (Chawla and Mujumdar, 2015; Li et al., 2024). Sustaining *WR* amid worsening water shortages and water quality degradation is increasingly challenging, while the relative contributions of climate and land-use changes remain poorly quantified in topographically complex transboundary basins (Chen et al., 2024).

Hydrological models and the Budyko framework are two commonly used approaches for hydrological attribution (Chawla and Mujumdar, 2015; Sharma and Mondal, 2022; Collignan et al., 2023). Hydrological models, including SWAT, VIC, WEP-L, and InVEST, are widely used to simulate hydrological processes and assess the impacts of climate and land-use changes on *WR*, owing to their flexibility across diverse climatic and topographic settings and their adaptability to region-specific hydrological conditions (Wang et al., 2021; Hua et al., 2025; Xu et al., 2026). However, their process representations, data requirements, and applicability differ depending on the research objectives and regional conditions. SWAT is suited to evaluating the impacts of management practices on water supply and nonpoint-source pollution but requires a large number of input parameters, complicating model parameterization and calibration (Arnold et al., 1998, 2012), whereas InVEST provides an accessible, spatially explicit approach to annual water-yield assessment but simplifies hydrological processes (Vigerstol and Aukema, 2011; Hamel and Guswa, 2015). VIC simulates gridded land-surface water and energy balances and can integrate ground observations and satellite data, making it suitable for large-scale *WR* assessment and future *WR* projections under climate-change scenarios, although its performance can be influenced by the quality and spatial representation of input data (Liang et al., 1994; Nguyen et al., 2018; Zhai et al., 2018).

Outputs from global climate models (GCMs) participating in the Coupled Model Intercomparison Project Phase 6 (CMIP6) provide scenario-based climate projections for assessing global and regional climate change (Brands, 2022; IPCC, 2023). To reduce systematic GCM biases and improve climate forcing for hydrological simulations, many studies have used bias-correction techniques to adjust GCM projections against observations (Cannon, 2018; Chae and Chung, 2024; Menapace et al., 2025). Commonly used approaches include the delta change method (Gleick, 1986), direct statistical downscaling (Maraun et al., 2010), and quantile mapping (QM) (Lange, 2019; Sun and Lan, 2020). In addition, multi-model ensemble approaches have been widely adopted to improve the robustness of climate projections and hydrological impact assessments (Liaqat et al., 2025; Woo et al., 2025). Common ensemble techniques include simple arithmetic averaging (Viney et al., 2009), weighted averaging methods (Guo et al., 2021), regression-based approaches (Jozaghi et al., 2021), and neural network–based ensemble methods (Shamseldin et al., 1997; Chiang et al., 2022). Together, these advances provide important technical pathways for projecting *WR* and related hydrological responses under alternative climate scenarios (Zhai et al., 2018; Yin et al., 2022). Nevertheless, integrated assessments combining historical attribution and future *WR* projections remain limited.

As a major transboundary river basin in Southeast Asia, the Yuanjiang–Red River Basin (YRRB) is important for regional water security, ecological sustainability, and cross-border water management. Previous YRRB studies have examined hydrological and sediment simulations (Ranzi et al., 2012; Nguyen et al., 2024), human influences on non-stationary hydrological drought in the upper basin (Leng et al., 2024), and CMIP6-based runoff and hydrological drought projections in the Yuanjiang River Basin (Dou et al., 2025). Other studies have addressed vegetation change (Zhang et al., 2025), reservoir operation optimization (Ngo et al., 2007), and downstream salinity-related water resources management (Nguyen et al., 2023b). However, long-term *WR* attribution, scenario-dependent *WR* projections, and spatial differences in *WR* responses among upstream and downstream sub-basins spanning China and Vietnam remain insufficiently examined in the YRRB. To address these gaps, this study employs a multi-model coupled framework integrating hydrological simulation, historical attribution, multi-model climate projections, and spatiotemporal pattern analysis. Specifically, this study aims to: (1) characterize the spatiotemporal evolution and long-term trends of *WR* across the whole basin and six sub-basins during 1973–2015; (2) quantify the relative contributions of climate and land-use changes to *WR* at both the whole-basin and individual sub-basin scales; and (3) project *WR* under three SSP scenarios for 2016–2050 and identify its dominant spatial patterns and corresponding temporal variations.

2. Materials and methods

2.1. Study area

The Yuanjiang–Red River Basin (YRRB) originates in Yunnan Province, southwestern China, and flows northwest–southeast

through four prefectures in Yunnan and northern Vietnam before discharging into the Gulf of Tonkin (Beibu Gulf) of the South China Sea. Spanning approximately 156,451 km^2, the basin is nearly evenly divided between China (48.8%) and Vietnam (50.3%), with only 0.9% in Laos (Le et al., 2007). Sub-basins I–III are located in the Chinese upper reaches, whereas sub-basins IV–VI are transboundary units whose areas lie mainly in Vietnam, with sub-basin IV also including a small part of Laos (Fig. 1). The YRRB has a subtropical monsoon climate, with precipitation as its primary water source and pronounced upstream–downstream heterogeneity (Gao et al., 2015). Precipitation decreases from south to north in China and is higher in mountainous areas than in valleys, whereas Vietnam generally receives more precipitation, reaching approximately 3000 mm in coastal regions (Nguyen et al., 2024). Mean monthly temperature varies spatially and seasonally, ranging from 14 to 27 °C upstream to 17–30 °C in the downstream delta. Topographically, the YRRB is a low-latitude mountainous river–valley system characterized by pronounced vertical relief and a mean elevation of 1162 m, descending from north to south. Land-management pathways differ between the Chinese and Vietnamese sectors. In China, the Natural Forest Protection Program and the Grain for Green Project have been implemented since the late 1990s and have influenced vegetation-cover patterns in the Chinese portion of the Red River Basin (Gu et al., 2018; Zhang et al., 2025). In Vietnam, deteriorating forest conditions led to the historical implementation of Programs 327 and 661 to reduce environmental degradation and promote forest regrowth (Trædal and Angelsen, 2020). Hydrologically, the YRRB exhibits strong seasonal variability in runoff, with a mean annual discharge of approximately 3500 m^3 s^{-1} at Son Tay (Fig. 1) (Dang et al., 2010), dry-season discharge decreasing to approximately 370 m^3 s^{-1} , and peak flows during the rainy season reaching around 38,000 m^3 s^{-1} (Nguyen et al., 2018). In this study, the YRRB was delineated into six sub-basins using key hydrological stations as control sections (Fig. 1).

2.2. Data

This study utilized multiple datasets to characterize the hydrological, meteorological, and geographical conditions of the basin. Observed monthly runoff data were collected from six hydrological stations located in the main stream and major tributaries across China and Vietnam. Meteorological forcing data, including precipitation, maximum/minimum temperature, and wind speed, were obtained from observation-based gridded datasets for the historical period (1973–2015), including the APHRODITE daily precipitation dataset (Asian Precipitation–Highly Resolved Observational Data Integration Towards Evaluation) and the Princeton Global Meteorological Forcing dataset. For the projection period (2016–2050), meteorological forcing data were derived from the downscaled projections of five GCMs (ACCESS-CM2, BCC-CSM2-MR, EC-Earth3, GFDL-ESM4, and MIROC6) obtained from the NEX-GDDP-CMIP6 dataset under multiple Shared Socioeconomic Pathway (SSP) scenarios. Additionally, spatial datasets, including elevation and historical and projected land-use/land-cover (LULC) data, were incorporated to support hydrological model setup and scenario simulations. Dataset variables, spatial resolutions, temporal coverage, and sources are summarized in Table S1. Further details on the rationales for selecting the five GCMs and using the 2030 LULC maps are provided in Supplementary Texts S1 and S2, respectively.

3. Methodology

Fig. 2 presents the overall framework of this study. First, spatiotemporal variations in key hydrological variables across the YRRB and its sub-basins are analyzed by coupling the VIC model with a water-balance approach. Second, the historical contributions of

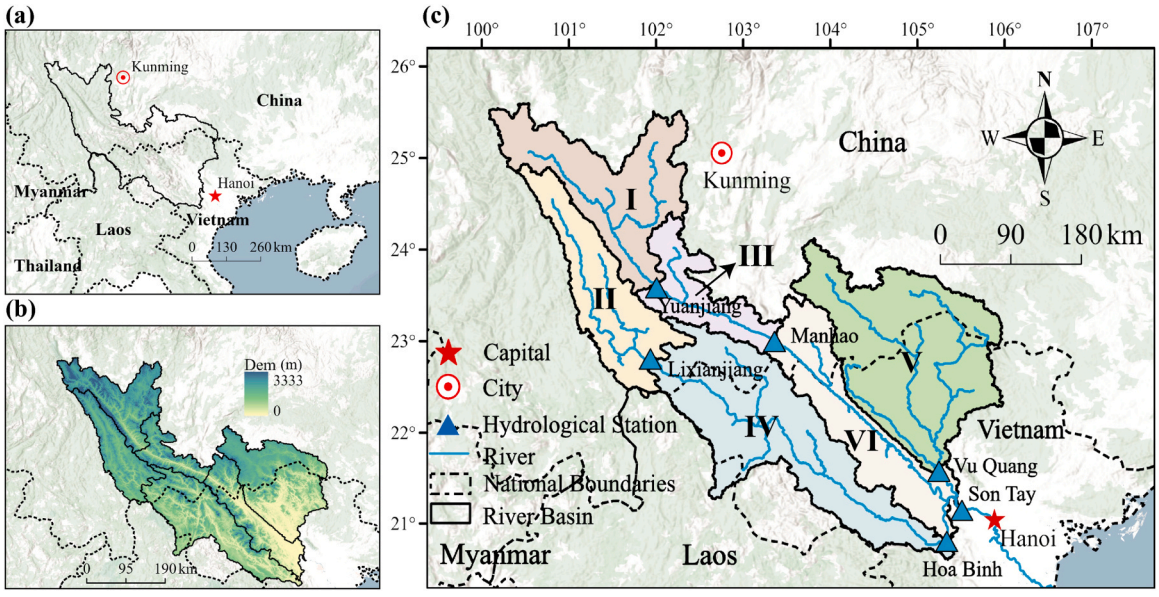


Fig. 1. (a) Location, (b) elevation, and (c) water systems, sub-basin delineation, and hydrological monitoring stations of the study area.

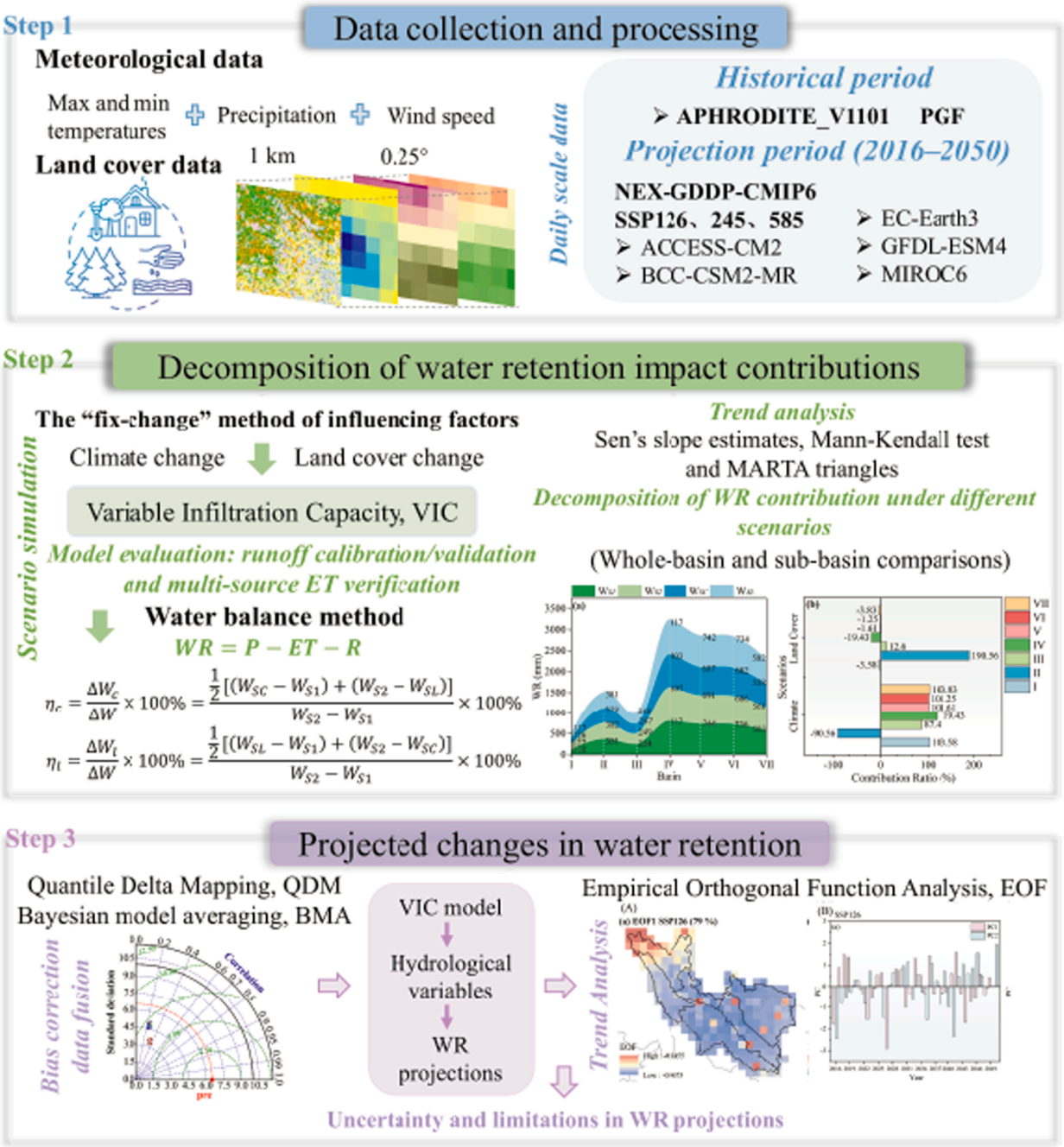


Fig. 2. Analytical framework for this study.

climate and land-use changes to *WR* are isolated and quantified. Third, outputs from multiple GCMs are bias-corrected using quantile delta mapping against the historical meteorological forcing used in the VIC simulations and are then integrated using Bayesian model averaging (BMA). The BMA-based meteorological forcing data for the projection period are then used to drive the VIC model to simulate hydrological variables and assess *WR* under the three SSP scenarios. Finally, empirical orthogonal function analysis is applied to the projected *WR* fields under the three SSP scenarios to identify the dominant spatial patterns and their associated temporal variations.

3.1. Hydrological simulation

The Variable Infiltration Capacity (VIC) model, a grid-based physical hydrological model, was employed to simulate coupled

water–energy processes across the study basin (Liang et al., 1994, 1996). The model was implemented at a 0.25° × 0.25° resolution to maintain consistency with the gridded meteorological datasets used in this study, with vegetation and soil parameterizations based on Nijssen et al. (2001a), (2001b). A one-year warm-up period (1972) was followed by calibration (1973–1982) and validation (1983–1993). Specifically, the 1993 LULC data were used during the calibration and validation periods to represent baseline land-surface conditions, whereas the 2015 LULC data were used for the simulation period (1994–2015) to reflect subsequent LULC changes. Ten key parameters were optimized using a genetic algorithm (GA; Holland, 1975) by maximizing the mean Nash–Sutcliffe efficiency (NSE) across the six stations (Table S2; Supplementary Text S3). Model performance was evaluated using the NSE, while the root mean square error (RMSE) and percent bias (PBIAS) were employed as complementary metrics to assess simulation accuracy (Althoff and Rodrigues, 2021).

For the historical period (1973–2015), precipitation was obtained from the APHRODITE gridded dataset, whereas actual evapotranspiration and surface runoff were obtained directly from the VIC model outputs on the 0.25° × 0.25° model grid. Given the spatial heterogeneity in hydroclimatic conditions across the basin, the study area was subdivided into six sub-basins based on the DEM using hydrological analysis tools in ArcGIS. This subdivision facilitated the assessment of spatial differences in W*R* among the sub-basins. For each of the six sub-basins and the entire basin, area-weighted mean precipitation, actual evapotranspiration, and surface runoff were calculated from all grid cells within the corresponding spatial unit. Based on the water balance principle, W*R* for each sub-basin and the entire basin was estimated as the residual of precipitation after accounting for actual evapotranspiration and surface runoff (Zhang et al., 2024a; Xu et al., 2026):

$$WR = P - ET - R \tag{1}$$

where W*R*, P, ET, and R denote water retention, precipitation, actual evapotranspiration, and surface runoff, respectively. The unit of each variable is mm.

3.2. Contribution decomposition of WR impact

Using a factor "fixing-varying" design (Xiao et al., 2023), the baseline period (P1, 1973–1993) and change period (P2, 1994–2015) were combined into four VIC scenarios to isolate the effects of climate and land-use changes on W*R* (Table 1).

Based on the scenario-based hydrological simulation results and the water balance approach, the contributions of climate change and land-use change to W*R* were separated using Eqs. (2)–(3) (Li et al., 2024).

$$\eta_c = \frac{\Delta W_c}{\Delta W} \times 100\% = \frac{\frac{1}{2}[(W_{SC} - W_{S1}) + (W_{S2} - W_{SL})]}{W_{S2} - W_{S1}} \times 100\% \tag{2}$$

$$\eta_l = \frac{\Delta W_l}{\Delta W} \times 100\% = \frac{\frac{1}{2}[(W_{SL} - W_{S1}) + (W_{S2} - W_{SC})]}{W_{S2} - W_{S1}} \times 100\% \tag{3}$$

where η_c and η_l denote the contribution rates of climate change and land-use change (%), respectively; ΔW_c, ΔW_l and ΔW denote the climate-induced, land-use-induced, and total changes in W*R* (mm), respectively. W_{S1}, W_{S2}, W_{SC} and W_{SL} represent W*R* under the corresponding scenarios (mm). Positive contribution rates indicate that the corresponding driver-induced change has the same sign as ΔW, whereas negative rates indicate the opposite sign.

3.3. Bias correction

The quantile delta mapping (QDM) method was introduced by Cannon et al. (2015) as a bias-correction approach designed to preserve model-projected changes in quantiles. Linear scaling primarily corrects biases in the mean (Teutschbein and Seibert, 2012), whereas conventional quantile mapping may alter the model-projected climate-change signal. Accordingly, QDM was selected for bias correction in this study.

In this study, QDM was implemented using the empirical cumulative distribution function (ECDF) to reduce potential additional uncertainty associated with fitting parametric distributions. The correction was applied separately to precipitation, maximum temperature, minimum temperature, and wind speed from each of the five GCMs, using 1973–2014 as the historical reference period. APHRODITE was used as the reference dataset for precipitation, whereas PGF was used for maximum temperature, minimum temperature, and wind speed. The QDM formulation and notation are provided in Supplementary Text S4.

Table 1
Scenario simulation design.

Scenario	Climate	LULC	Response	Description
S_1	P1	P1	W_{S1}	Baseline climate and LULC
S_2	P2	P2	W_{S2}	Changed climate and LULC
S_C	P2	P1	W_{SC}	Changed climate with baseline LULC
S_L	P1	P2	W_{SL}	Baseline climate with changed LULC

3.4. Bayesian model averaging

To account for inter-model uncertainty in climate projections, Bayesian model averaging (BMA), which combines individual model predictions using their posterior model probabilities (Raftery et al., 2005), was applied to integrate the QDM-corrected projections from five GCMs. The BMA ensemble prediction was calculated as follows:

$$y_{BMA} = \sum_{k=1}^{K} p(M_k|D) y_{M_k} \tag{4}$$

where M_k denotes the k-th GCM, D denotes the historical training data, y_{M_k} is the prediction of M_k, $p(M_k|D)$ is its posterior probability given D, K is the total number of models, and y_{BMA} is the BMA ensemble prediction.

For each meteorological variable, the BMA weights and variance parameters were estimated from the historical training data by maximizing the log-likelihood function. The weights reflect the relative predictive performance of the five GCMs after QDM correction and were subsequently applied to the corresponding bias-corrected projections under each SSP scenario. Temperature was assumed to follow a Gaussian distribution, whereas precipitation and wind speed were log-transformed as $\log(x + \varepsilon)$ to satisfy the distributional assumptions.

3.5. Empirical Orthogonal Function analysis

Empirical orthogonal function (EOF) analysis extracts dominant modes of variability by decomposing spatiotemporal datasets into orthogonal spatial patterns and their associated temporal coefficients (Dommenget and Latif, 2002). It has been widely used to characterize river-basin flow variability and spatiotemporal hydrological dynamics (Lai et al., 2021; Nguyen et al., 2023a). The mathematical formulation is as follows:

$$C = XX^T = (VT)(VT)^{\mathrm{T}} = V\Lambda V^{\mathrm{T}} \tag{5}$$

where X is the resulting spatiotemporal WR matrix, C is its spatial covariance matrix, V is the matrix of spatial eigenvectors, Λ is the diagonal matrix of corresponding eigenvalues, and the superscript T denotes matrix transpose. The eigenvalues determine the variance explained by each EOF mode. The temporal coefficient matrix T is obtained by projecting X onto V, allowing X to be expressed as the product of V and T:

$$T = V^{\mathrm{T}}X \tag{6}$$

$$X = VT \tag{7}$$

4. Results

4.1. Model calibration and validation

Table 2 summarizes runoff calibration and validation. Validation performance was comparable between the Chinese and Vietnamese stations, with NSE exceeding 0.83 at all stations. For the Chinese stations (Yuanjiang, Manhao, and Lixianjiang), RMSE values ranged from 68.5 to 124.0 $m^3 s^{-1}$, while PBIAS remained within −20.15% to + 3.69%. At the Vietnamese stations (Son Tay, Hoa Binh, and Vu Quang), PBIAS ranged from −11.01% to −0.045%, and RMSE was 886.3, 582.8, and 326.5 $m^3 s^{-1}$, respectively. According to the monthly performance criteria proposed by Moriasi et al. (2007), the runoff simulation performance can be classified as "good". VIC-simulated actual evapotranspiration (ET) was compared with GLEAM4 (Miralles et al., 2025) (1980–2015), TerraClimate (Abatzoglou et al., 2018) (1973–2015), and SiTHv2 (Zhang et al., 2024b) (1982–2015). Spatial correlations were generally moderate to high, with values mainly ranging from 0.41 to 0.80, 0.61–0.93, and 0.41–0.91, respectively, while lower correlations occurred only in limited areas (Fig. S1). Overall, the model evaluation suggests that the calibrated model is suitable for the long-term simulation of hydrological variables in the YRRB.

Table 2
Basic information of six hydrological stations and VIC model performance for monthly runoff simulation in the YRRB.

Stations	Area (km^2)	Calibration period (1973–1982)				Validation period (1983–1993)			
		NSE	RMSE ($m^3 s^{-1}$)	PBIAS (%)	Mean ($m^3 s^{-1}$)	NSE	RMSE ($m^3 s^{-1}$)	PBIAS (%)	Mean ($m^3 s^{-1}$)
Yuanjiang	21,583	0.84	56.8	-5.92	137	0.84	68.5	-7.89	147
Lixianjiang	16,949	0.80	139.0	-24.36	269	0.84	124.0	-20.15	273
Manhao	31,597	0.89	71.2	2.67	263	0.89	79.2	3.69	284
Hoa Binh	50,715	0.91	419.1	-7.91	1487	0.83	582.8	-11.01	1374
Vu Quang	35,848	0.85	305.9	5.17	1128	0.84	326.5	-0.045	1066
Son Tay	136,911	0.94	692.1	-2.63	3451	0.89	886.3	-2.78	3238

4.2. Spatiotemporal evolution of key hydrological variables

As summarized in Table 3, the YRRB exhibits spatial heterogeneity: the upper reaches (sub-basins I–III) are characterized by relatively lower precipitation and higher evaporative demand, whereas downstream sub-basins (IV–VI) receive abundant precipitation and exhibit high W*R*. Despite this spatial heterogeneity, the Mann–Kendall test for 1973–2015 revealed a generally consistent degradation pattern across the basin. Precipitation (P), runoff (R), and W*R* showed declining trends, whereas ET exhibited a slight increase. W*R* declines were weaker in the upper sub-basins, with Sen's slopes ranging from −1 to −13 mm decade^{-1} , than in the downstream sub-basins, where slopes ranged from −18 to −29 mm decade^{-1} . Sub-basin V exhibited the strongest and only statistically significant W*R* decline ($p < 0.05$).

Moving Average Running Trend Analysis (MARTA; Fig. 3) was applied to basin-wide averages over windows ranging from interannual to 43-year scales to characterize multi-scale temporal non-stationarity (Ranzi et al., 2024, 2025). MARTA reveals that P exhibited interannual-to-decadal variability, characterized by higher precipitation in the early-to-mid 1990s and reduced levels after the late 2000s (Fig. 3a). Meanwhile, ET shifted to a higher regime in 1996 at the basin scale (Fig. 3b). Sub-basin MARTA results showed no significant ET change points in upper sub-basins I–III, whereas significant shifts to higher ET levels were detected in downstream sub-basins IV–VI between 1996 and 1998 (Figs. S2–S7), consistent with the contrasting ET trends shown in Table 3. In contrast, R and W*R* generally declined after the late 1990s, but significant decreases were localized and scale-dependent rather than persistent across all windows (Fig. 3c–d). These results suggest that the recent decline in W*R* is associated with the combined effects of reduced precipitation availability and generally elevated ET after the mid-1990s, although the hydrological response remains temporally heterogeneous.

4.3. Contribution decomposition

Fig. 4 presents the mean W*R*, relative contribution rates, and absolute driver-induced W*R* changes across sub-basins under different scenarios. At the basin scale, mean annual W*R* under the change-period ($W_{S2} = 561$ mm), climate-only ($W_{SC} = 558$ mm), and land-use-only ($W_{SL} = 582$ mm) scenarios all remained below that of the baseline-period scenario ($W_{S1} = 583$ mm) (Fig. 4a). Relative to the baseline period, basin-wide W*R* decreased by 3.81% during the change period, with larger declines downstream (Table 4). Specifically, downstream sub-basin V exhibited the largest decline (7.14%), whereas upstream sub-basins I and II showed increases of 7.45% and 0.25%, respectively. The relatively large percentage increase in sub-basin I partly reflected its low baseline W*R*. Comparing driving scenarios reveals that climate-induced W*R* changes were generally larger than land-use-induced changes across most sub-basins, with generally consistent change directions. Under the climate change scenario, sub-basin V experienced the largest decrease (7.57%) relative to the baseline, while only sub-basin I showed a slight increase (6.70%). In contrast, W*R* changes under the land-use change scenario were limited across sub-basins, indicating that land-use change alone had a relatively weak effect on W*R*. This pattern is further supported by the absolute driver-induced changes in Fig. 4b. In particular, land-use change in sub-basin II increased W*R* by approximately 1.82 mm, partly offsetting the climate-induced decrease of approximately 0.87 mm.

The contribution decomposition analysis further clarified the relative roles of climate and land-use changes, revealing that the basin-wide decline in W*R* was primarily driven by climate change (Fig. 4c). With a contribution rate of 103.83%, climate change acted as the dominant driver, offsetting the modest mitigating effect of land-use change ($\eta_l = -3.83\%$). Although climate effects dominated in most sub-basins, W*R* responses varied spatially. Land-use change buffered W*R* in upstream sub-basin II, located in China, whereas climate change dominated W*R* declines in downstream sub-basins V−VI, located mainly in Vietnam. Specifically, climate consistently drove W*R* degradation in sub-basins III–VI, with sub-basin III experiencing a compounded dual penalty from both land use ($\Delta W_l =$ –1.96 mm, $\eta_l = 12.60\%$) and climate ($\Delta W_c =$ –13.63 mm, $\eta_c = 87.40\%$). Conversely, climatic differences between the baseline and change periods led to a slight average W*R* increase in sub-basin I ($\Delta W_c = 9.13$ mm, $\eta_c = 103.58\%$), although this period-to-period shift does not negate the long-term declining trend in W*R* shown in Table 3. Although the land-use contribution rate in sub-basin II reached 190.56%, the corresponding absolute W*R* increase was only 1.82 mm (Fig. 4b). The contribution rate represents the relative share of land-use change in the small net W*R* change, whereas the absolute change represents the actual magnitude of the W*R* response. Therefore, the large percentage does not imply a large absolute land-use effect.

Table 3
Multi-year mean values, Sen's slope estimates, and Mann–Kendall test results for key hydrological variables in the six sub-basins and the entire basin during the historical period (1973–2015). * and ** indicate statistical significance at $p < 0.05$ and $p < 0.01$, respectively.

Basin	P			ET			R			W*R*		
	Mean	Slope	Z-value	Mean	Slope	Z-value	Mean	Slope	Z-value	Mean	Slope	Z-value
I	858	-14	-0.98	639	-11	-1.40	96	-1	-0.50	123	-1	-0.08
II	1214	-21	-1.07	698	-8	-1.78	135	-3	-0.92	381	-8	-0.63
III	1020	-17	-1.19	584	-2	-0.52	180	-6	-1.26	256	-13	-1.44
IV	1610	-8	-0.44	496	17	3.85**	301	-5	-1.07	812	-18	-1.28
V	1370	-30	-1.47	414	7	2.45*	239	-9	-1.53	717	-29	-2.11*
VI	1498	-26	-1.13	513	16	3.68**	274	-13	-1.80	711	-28	-1.90
YRRB	1322	-18	-1.13	531	5	1.61	220	-6	-1.26	572	-18	-1.86

Note: P was obtained from APHRODITE, ET and R were simulated by VIC, and W*R* was derived using Eq. (1). Mean values (mm) and slope (mm decade^{-1}).

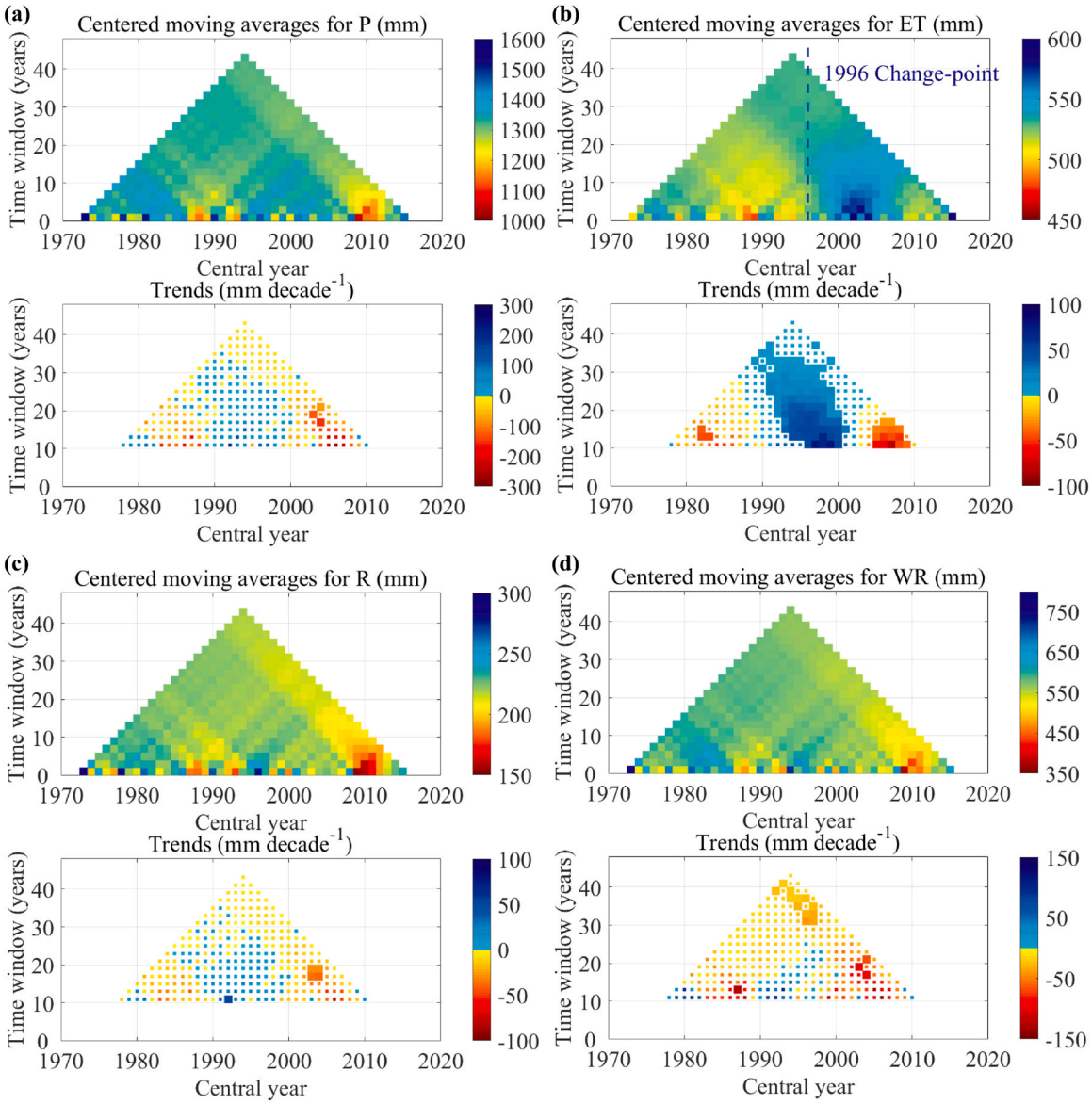


Fig. 3. MARTA triangles of (a) precipitation, (b) actual evapotranspiration, (c) surface runoff, and (d) W*R* for the entire YRRB. Dashed lines indicate change points identified by the Pettitt test ($p < 0.05$), and thicker pixels denote significant trends detected by the Mann–Kendall test ($p < 0.05$).

4.4. Evaluation of QDM-corrected and BMA-integrated meteorological forcing

The five QDM-corrected GCMs and the corresponding BMA estimates were evaluated against APHRODITE and PGF over 1973–2014 using Taylor diagrams. Because QDM and BMA were applied separately to each meteorological variable, the evaluation focused on the meteorological inputs. Results for precipitation and temperature are shown in Fig. 5, and those for wind speed in Fig. S8. For precipitation, correlations of individual GCMs remained relatively low (0.23–0.25) (Fig. 5a). The BMA ensemble increased the correlation to 0.33 and reduced the centered root-mean-square error (cRMSE) to 6.29 mm. Its standard deviation was 3.55 mm (SD ratio = 0.55), indicating lower variability than the reference dataset. Temperature simulations exhibited higher correlations and lower cRMSE values than precipitation. QDM-corrected GCMs yielded correlations of 0.71–0.73 for maximum temperature and 0.85–0.88 for minimum temperature (Fig. 5b–c). The BMA ensemble further increased the correlations to 0.80 and 0.91, respectively, while reducing the cRMSE values. Relative to the individual GCM ranges, BMA increased the correlation by 0.08–0.10 for precipitation, 0.07–0.09 for maximum temperature, and 0.03–0.06 for minimum temperature. Overall, the BMA estimates generally agreed more closely with the reference datasets than the individual QDM-corrected GCM simulations and were therefore used to construct the meteorological forcing for the VIC projections.

Historical gridded observations and BMA projections indicate that the slight historical precipitation decline will persist across all

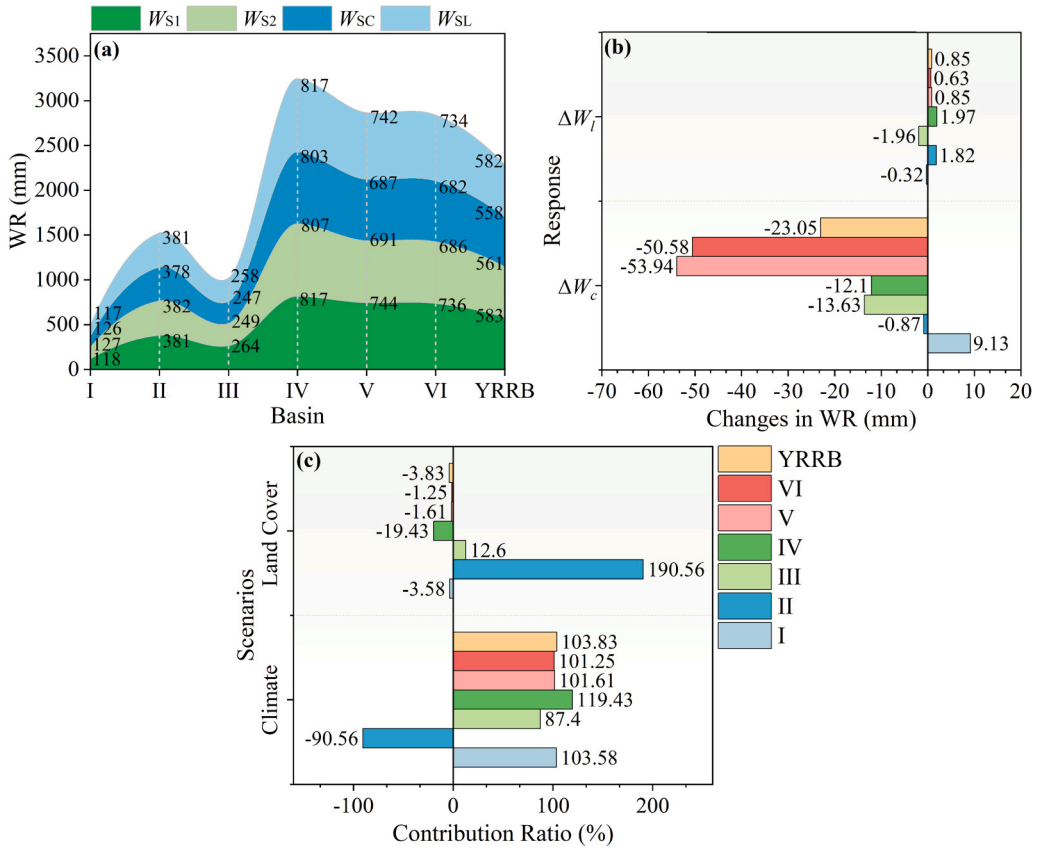


Fig. 4. Historical attribution of W*R* across the six sub-basins and the entire basin: (a) multi-year mean W*R* under the S_1, S_2, S_C, and S_L scenarios; (b) absolute W*R* changes induced by climate change (ΔW_c) and LULC change (ΔW_l); and (c) the corresponding contribution rates (η_c and η_l).

Table 4
Percent change in W*R* relative to the baseline period across different scenarios (%).

Scenario/Basin	I	II	III	IV	V	VI	YRRB
S_2-S_1 (Climate and LULC)	7.45	0.25	-5.90	-1.24	-7.14	-6.79	-3.81
S_C-S_1 (Climate)	6.70	-0.67	-6.72	-1.80	-7.57	-7.29	-4.36
S_L-S_1 (LULC)	-1.28	0.04	-2.30	-0.08	-0.20	-0.33	-0.26

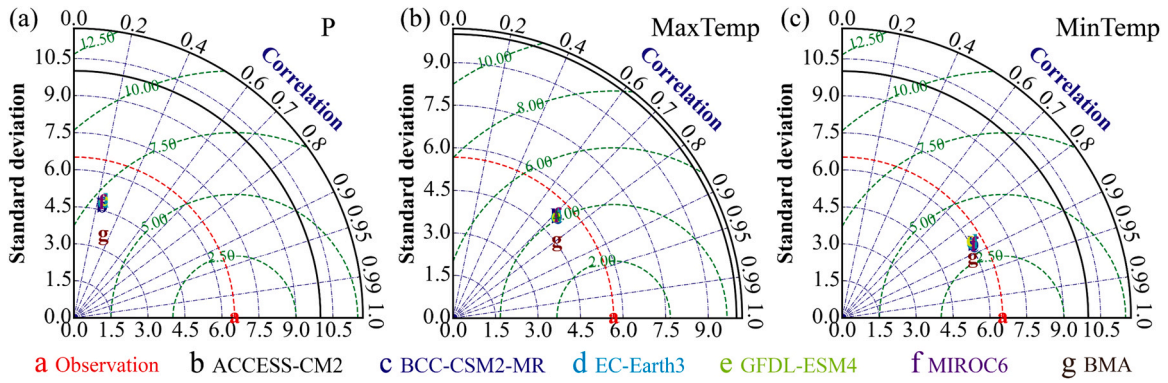


Fig. 5. Taylor diagram of daily precipitation (P), maximum temperature (MaxTemp), and minimum temperature (MinTemp) for five QDM-corrected GCMs and their BMA ensemble in the YRRB (1973–2014). The standard deviation is indicated by the radial distance from the origin, the correlation coefficient by the angular position and blue arcs, and the cRMSE by the green dashed lines.

projection scenarios (Fig. 6a). The largest decrease was projected under SSP585 (7.10%), whereas the decreases under SSP126 (5.92%) and SSP245 (5.86%) differed only marginally, indicating similar precipitation changes under these two scenarios. Both maximum and minimum temperatures are projected to increase continuously through the projection period (Fig. 6b–c). Warming magnitudes were relatively similar under SSP126 and SSP245 but were larger under SSP585, where maximum and minimum temperatures are projected to increase by 1.52 °C and 1.72 °C, respectively. Notably, minimum temperature showed a greater warming response under higher forcing. Its projected warming magnitude increased from 1.59 °C under SSP126–1.72 °C under SSP585.

4.5. Projected trends in WR under the SSP scenarios

Fig. 7 illustrates the projected shifts in mean annual hydrological variables across the YRRB. Under SSP scenarios, precipitation is projected to decline slightly, whereas evapotranspiration (ET) is expected to increase by 31.4%–34.3% under a warming climate (Fig. 7b). This combination of reduced precipitation and increased ET contributes to a marked decline in runoff, with losses reaching 34.2%–37.2% (Fig. 7c). Reflecting this systemic stress, *WR* is projected to decline consistently, with long-term averages decreasing by 29.6%–33.5% (Fig. 7d). These results highlight a hydrological pattern of slight precipitation loss coupled with intensified evapotranspiration, suggesting that increasing atmospheric water demand may place growing pressure on regional *WR* services.

The first two EOF modes jointly explained 80%–86% of the total variance across the three SSP scenarios and were therefore retained as the dominant spatial modes of projected *WR* (Fig. 8). The separability of these modes was assessed using North's rule of thumb (Text S5). EOF1 exhibits a basin-wide monopolar structure with loadings of the same sign across the basin. Loading magnitudes increased from upstream to downstream, indicating a stronger contribution in the lower reaches. Under SSP245 and SSP585, the EOF1 spatial loadings are uniformly positive, whereas the corresponding PC1 values are predominantly negative. EOF2 captures regional contrasts, with spatial patterns varying among scenarios. EOF2 exhibits an upstream–downstream dipole pattern under all three scenarios, indicating out-of-phase *WR* variability between the upper and lower basin. EOF1 explained 79%, 64%, and 68% of the variance under SSP126, SSP245, and SSP585, respectively, whereas EOF2 explained 7%, 17%, and 12%. Compared with SSP126, the reduced contribution of EOF1 and increased contribution of EOF2 under SSP245 and SSP585 indicate weaker basin-wide coherence and greater regional differentiation.

5. Discussion

5.1. Impacts of land use and climate change on WR

Climate change is the dominant driver of *WR* decline, with land-use change exerting localized buffering effects (Fig. 4; Table 4).

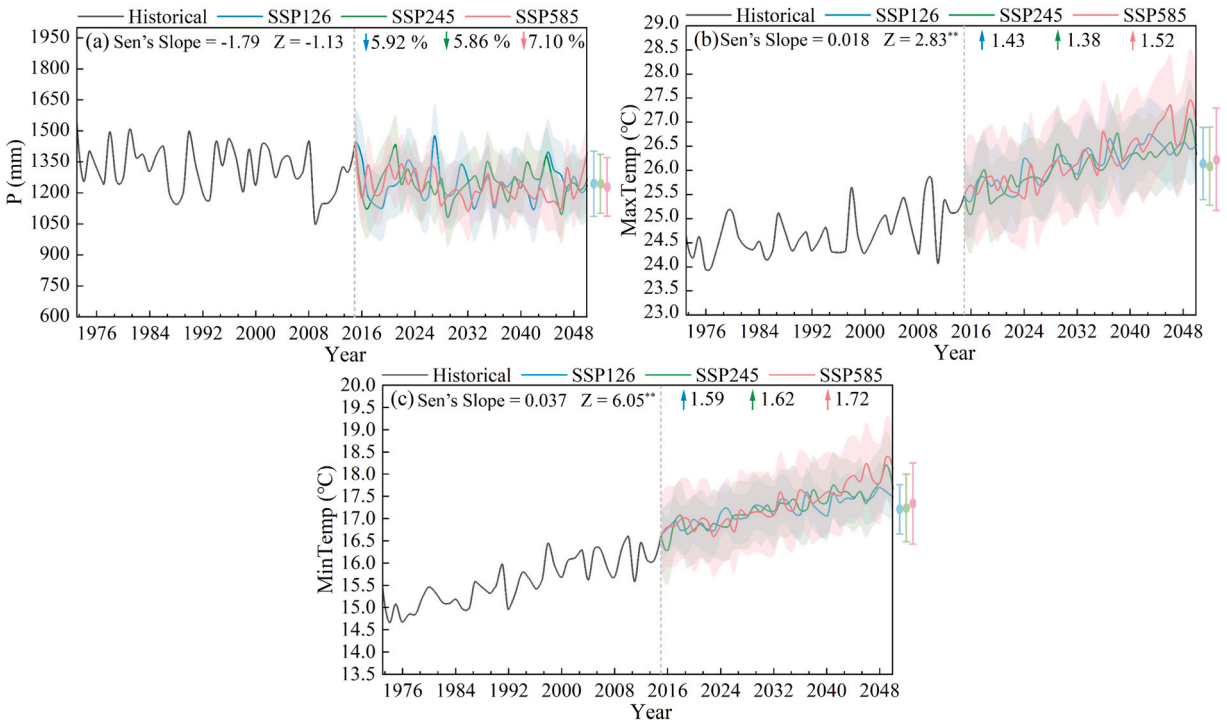


Fig. 6. Historical and BMA-based projected annual variations in (a) P, (b) MaxTemp, and (c) MinTemp in the YRRB under three SSP scenarios. Slopes are expressed in mm yr^{-1} and °C yr^{-1} . Values marked with ** are significant at $p < 0.01$.

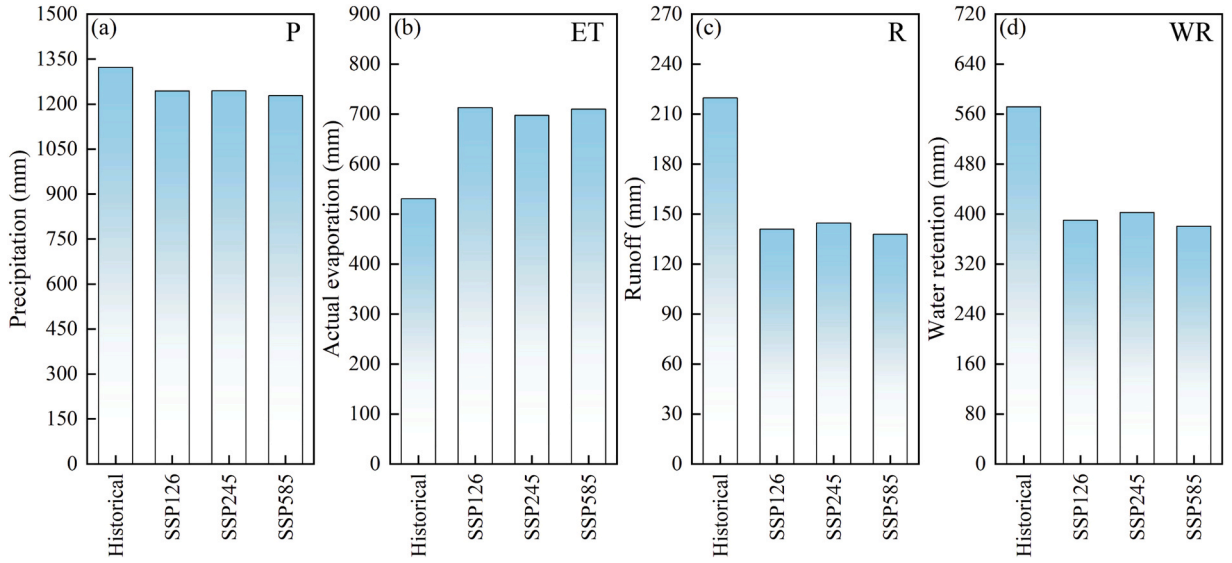


Fig. 7. Mean annual values of (a) precipitation, (b) actual evapotranspiration, (c) surface runoff, and (d) *WR* in the YRRB during the historical period and under the SSP projection scenarios.

Previous studies have generally reported stronger climatic than land-use influences on *WR*, although land-use effects may remain important locally. Across China, climate change, particularly precipitation change, exerted a greater influence on terrestrial ecosystem *WR*, whereas the effects of LULC change were generally smaller (Zhai and Tao, 2021). In Southeast Asia, directly comparable studies separating climate and LULC contributions to *WR* remain limited. Nevertheless, water yield in the Lancang–Mekong River Basin declined and was strongly influenced by precipitation (Liu et al., 2025). Within the YRRB, MARTA provides complementary temporal context for the scenario-based attribution, showing that generally declining trends in R and *WR* coincided with reduced precipitation availability and elevated ET (Table 3; Fig. 3).

Land-use effects were spatially heterogeneous, with limited buffering in sub-basin II (Fig. 4). Forest-protection and restoration programs have been implemented in both China and Vietnam, although their spatial outcomes differ across the basin (Gu et al., 2018; Trædal and Angelsen, 2020; Zhang et al., 2025; FAO, 2025). The Chinese portion contains 57.04% of the basin's forestland and accounts for 53.09% of its forest expansion (Fig. S9), which may have contributed to the localized buffering effect in sub-basin II. In downstream sub-basins V and VI, modeled land-use effects remained small relative to the climate-driven *WR* declines. At the basin scale, these effects were insufficient to reverse the climate-driven *WR* decline. Future studies should isolate the effects of individual LULC conversions and spatial configuration.

5.2. *Differential responses of WR to projection scenarios*

Projected *WR* responses exhibit scenario-dependent variations in magnitude and spatial structure (Figs. 7–9). With relatively small precipitation changes but consistently elevated evapotranspiration under stronger radiative forcing, *WR* dynamics are increasingly dominated by atmospheric demand rather than precipitation supply (Fig. 9). From a water-balance perspective, this asymmetric response between water inputs and atmospheric demand constrains effective runoff generation across much of the basin. Even where precipitation changes are weak or statistically insignificant, increasing evapotranspiration reduces water availability and contributes to the decline in *WR*. Despite higher baseline precipitation in the downstream basin, projected increases in ET may reduce this water-supply advantage and contribute to the spatial differentiation of *WR*. Such warming-induced evaporative demand is widely recognized as a key mechanism intensifying drought and hydrological stress under climate change (Dai, 2012; Trenberth et al., 2013; IPCC, 2023; Ranzi et al., 2025). Beyond trend magnitudes, the EOF analysis further reveals structural differences in spatial organization among scenarios (Fig. 8). Under SSP126 and SSP585, projected *WR* exhibits relatively coherent basin-wide spatial patterns, whereas SSP245 shows greater spatial differentiation. *WR* evolution appears not to follow a simple monotonic response to scenario forcing, but instead involves a relative strengthening of the regional mode under SSP245 and SSP585, while the basin-wide mode remains dominant.

To further link these structural patterns with underlying physical processes, Pearson correlation analyses were conducted between EOF modes and trends in primary hydroclimatic variables (Table 5). The results demonstrate that the physical mechanisms governing the spatial evolution of *WR* exhibit significant divergence under varying radiative forcing. Across all scenarios, the regional mode (EOF2) shows a consistently significant spatial correlation with trends in ET ($|r| = 0.72$–0.90, $p < 0.01$), indicating that EOF2 likely reflects the localized influence of warming-driven land-surface thermodynamic processes on water cycle patterns. In contrast, the basin-wide mode (EOF1) shows scenario-dependent relationships: correlations with individual drivers are weak under SSP126 and SSP245, but become highly significant for both precipitation ($|r| = 0.76$) and ET ($|r| = 0.64$) under SSP585 ($p < 0.01$). This transition suggests that, under intensified warming, *WR* evolution may shift from relatively single-forcing control to a compound "double-

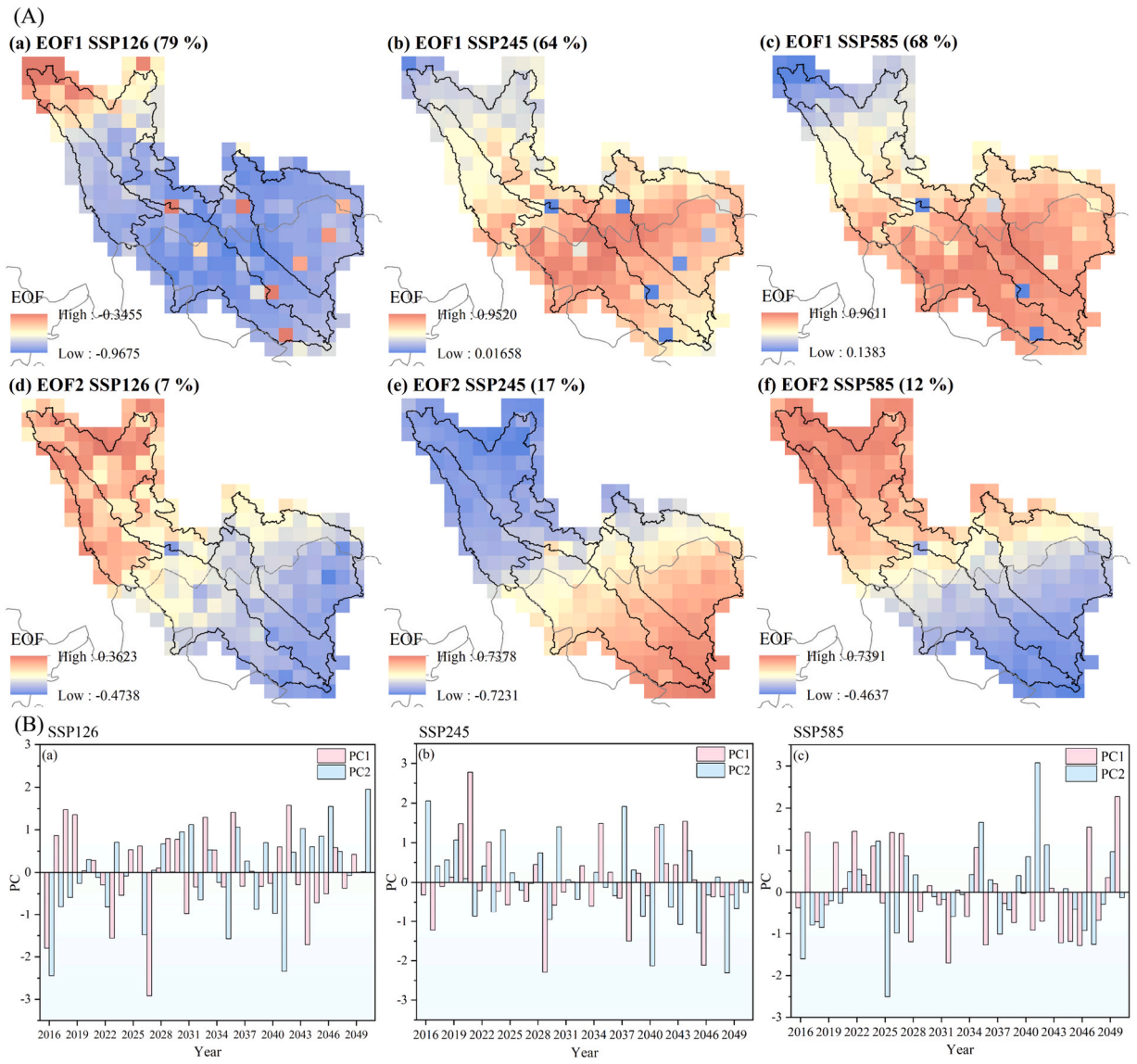


Fig. 8. Spatiotemporal characteristics of projected W*R* based on EOF analysis: (A) spatial patterns of EOF1 and EOF2 under SSP126, SSP245, and SSP585, with percentages indicating the explained variance; and (B) the corresponding PC1 and PC2 time series.

squeeze" mechanism driven by fluctuating water supply and rising atmospheric demand. The weakening of EOF1 and strengthening of EOF2 may further increase spatial differentiation, indicating that uniform basin-wide measures may be insufficient and that coordinated transboundary governance and differentiated upstream–downstream management may be needed.

5.3. Uncertainty and limitations in WR projections

The historical attribution analysis indicated that differences between the 1993 and 2015 LULC conditions resulted in a modeled W*R* increase of approximately 2 mm in sub-basins II and IV (Fig. 4). This estimate reflects the combined hydrological response to the overall differences between the LULC conditions used for the baseline and change periods, represented by the 1993 and 2015 LULC maps, rather than the effect of any individual land-cover transition. Temporal changes in LULC were not dynamically represented in the future projections. Because future land-use trajectories remain highly uncertain owing to unpredictable socioeconomic development, policy implementation, and societal behavior, particularly in rapidly urbanizing regions (O'Connell, 2017), the 2030 LULC map was adopted as a representative land-surface condition for the 2016–2050 period. Consequently, the projected W*R* trends primarily capture responses to time-varying climate forcing, while the potential effects of land-use changes after 2030 are not explicitly considered. In addition, the hydrological sub-basins do not fully coincide with national boundaries, which limits strict country-level comparisons between China and Vietnam. Future studies could adopt country-specific spatial delineation to support more rigorous

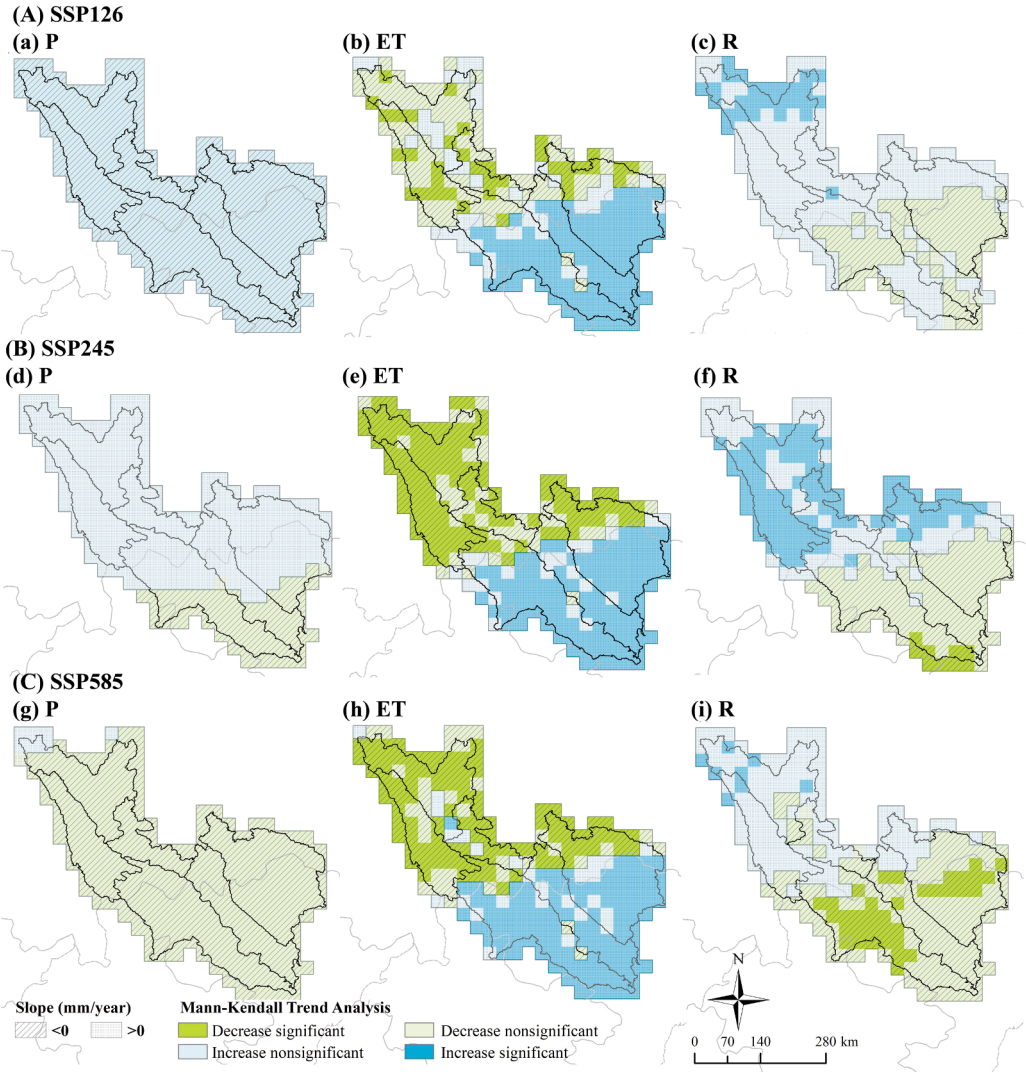


Fig. 9. Spatiotemporal trends in precipitation (P), actual evapotranspiration (ET), and runoff (R) in the YRRB under three climate scenarios. Panels (A–C) show SSP126, SSP245, and SSP585, respectively; subpanels (a, d, g), (b, e, h), and (c, f, i) correspond to P, ET, and R.

Table 5
Spatial correlations between EOF modes and trends in primary hydroclimatic variables across projection scenarios.

Scenario	Mode	P	ET
SSP126	EOF1	0.29**	0.20**
	EOF2	0.29**	0.72**
SSP245	EOF1	0.05	0.44**
	EOF2	0.67**	0.90**
SSP585	EOF1	0.76**	0.64**
	EOF2	0.90**	0.84**

Note: Due to the inherent sign indeterminacy of EOF analysis, Pearson correlation coefficients are presented as absolute values (|r|), reflecting the strength of spatial correspondence between EOF modes and hydroclimatic variables. ** indicates statistical significance at the 0.01 level ($p < 0.01$).

national-scale assessments.

Despite QDM bias correction and BMA integration, GCM structural differences in climate variables, particularly precipitation and temperature, remain an important source of uncertainty and may propagate into VIC simulations (Wang et al., 2020). The present framework focused on ensemble projections rather than independently isolating the effects of GCM structural differences, alternative

projected LULC pathways, and VIC parameter uncertainty. Their respective contributions to W*R* projection uncertainty could therefore not be quantitatively partitioned. Future studies could combine individual GCM-driven simulations, high-resolution and time-varying LULC projections, VIC parameter ensembles, and multiple hydrological or land-surface models to quantify their impacts more systematically.

The current VIC configuration did not explicitly represent domestic and industrial water withdrawals, irrigation water use, groundwater abstraction, or reservoir regulation. Water use, particularly irrigation withdrawals, can strongly affect low-flow conditions and amplify hydrological drought, while limited water-use data constrain rigorous attribution (Montanari et al., 2023). The effects of these omitted processes could therefore not be quantified separately, introducing uncertainty into the attribution results. Future studies should incorporate human water-use and management processes to better assess anthropogenic influences on W*R*.

The evaluation of the postprocessed forcing was conducted primarily at the meteorological-input level, and the propagation of residual forcing biases through VIC was not assessed separately. Because internal climate variability in free-running historical GCM simulations is not necessarily temporally synchronized with observations, direct month-to-month discharge comparisons may also reflect differences in temporal phasing (Maraun and Widmann, 2018). Future studies could further assess this uncertainty through a discharge-based impact-chain assessment.

6. Conclusion

This study assessed historical W*R* changes, quantified the contributions of climate and LULC changes, and projected W*R* under three SSP scenarios in the YRRB. Historical attribution showed that the basin-wide W*R* decline was mainly influenced by climate change, whereas the effects of land-use change were relatively weak and exhibited spatial heterogeneity. Ecological protection and vegetation restoration in the western and southwestern parts of the YRRB may have locally enhanced W*R* and partially buffered its decline. Across the three SSP scenarios, basin-mean W*R* is consistently projected to decline, although the magnitude and spatial organization of the changes vary among scenarios. The weakening of EOF1 and strengthening of EOF2 indicate reduced basin-wide coherence and enhanced regional differentiation, which may be associated with fluctuating precipitation supply and increasing evapotranspiration demand.

These findings may provide a reference for transboundary W*R* management. Basin-wide climate dominance, localized land-use buffering, and greater regional differentiation under higher-forcing scenarios suggest that climate adaptation, ecological protection, and sub-basin-specific W*R* assessment may warrant consideration in coordinated transboundary management. Improved communication between China and Vietnam regarding hydrometeorological and land-cover information could support coordinated monitoring and the future evaluation of management options. Because reservoir regulation and cross-border water-allocation processes were not explicitly represented in the current framework, future studies could further refine the assessment by incorporating these processes, multi-model ensembles of hydrological or land-surface models, high-resolution and time-varying LULC projections, and scenario-based modeling of transboundary ecological compensation.

CRediT authorship contribution statement

Yi Zou: Writing – review & editing, Writing – original draft, Visualization, Validation, Investigation, Funding acquisition, Data curation, Conceptualization. **Roberto Ranzi:** Writing – review & editing, Writing – original draft. **Xuan Ji:** Methodology, Investigation, Data curation. **Paolo Colosio:** Visualization, Validation, Methodology. **Nguyen Hao Quang:** Data curation. **Xuan Luo:** Visualization, Investigation. **Fan Zhou:** Visualization, Validation. **Jianxing Li:** Visualization. **Yungang Li:** Writing – review & editing, Supervision, Funding acquisition, Conceptualization.

Declaration of Competing Interest

The authors declare that they have no known competing financial interests or personal relationships that could have appeared to influence the work reported in this paper.

Acknowledgements

This work was supported by Yunnan Fundamental Research Projects (grant No. 202503AP140045) and China Scholarship Council.

Appendix A. Supporting information

Supplementary data associated with this article can be found in the online version at doi:10.1016/j.ejrh.2026.104001.

Data availability

The data that support the findings of this study are available from the corresponding author upon reasonable request.

References

Abatzoglou, J.T., Dobrowski, S.Z., Parks, S.A., Hegewisch, K.C., 2018. TerraClimate, a high-resolution global dataset of monthly climate and climatic water balance from 1958-2015. Sci. Data 5, 170191. https://doi.org/10.1038/sdata.2017.191.

Althoff, D., Rodrigues, L.N., 2021. Goodness-of-fit criteria for hydrological models: Model calibration and performance assessment. J. Hydrol. 600, 126674. https://doi.org/10.1016/j.jhydrol.2021.126674.

Arnold, J.G., Moriasi, D.N., Gassman, P.W., Abbaspour, K.C., White, M.J., Srinivasan, R., Santhi, C., Harmel, R.D., Van Griensven, A., Van Liew, M.W., 2012. SWAT: Model use, calibration, and validation. Trans. ASABE 55, 1491–1508. https://doi.org/10.13031/2013.42256.

Arnold, J.G., Srinivasan, R., Muttiah, R.S., Williams, J.R., 1998. Large area hydrologic modeling and assessment part I: Model development. J. Am. Water Resour. Assoc. 34, 73–89. https://doi.org/10.1111/j.1752-1688.1998.tb05961.x.

Brands, S., 2022. A circulation-based performance atlas of the CMIP5 and 6 models for regional climate studies in the Northern Hemisphere mid-to-high latitudes. Geosci. Model. Dev. 15, 1375–1411. https://doi.org/10.5194/gmd-15-1375-2022.

Cannon, A.J., 2018. Multivariate quantile mapping bias correction: an N-dimensional probability density function transform for climate model simulations of multiple variables. Clim. Dyn. 50, 31–49. https://doi.org/10.1007/s00382-017-3580-6.

Cannon, A.J., Sobie, S.R., Murdock, T.Q., 2015. Bias correction of GCM precipitation by quantile mapping: How well do methods preserve changes in quantiles and extremes? J. Clim. 28, 6938–6959. https://doi.org/10.1175/jcli-d-14-00754.1.

Chae, S.T., Chung, E.-S., 2024. Significant contribution of bias correction methods to uncertainty in future runoff projections under CMIP6 climate change. J. Hydrol. Reg. Stud. 56, 101973. https://doi.org/10.1016/j.ejrh.2024.101973.

Chawla, I., Mujumdar, P.P., 2015. Isolating the impacts of land use and climate change on streamflow. Hydrol. Earth Syst. Sci. 19, 3633–3651. https://doi.org/10.5194/hess-19-3633-2015.

Chen, G., Zuo, D., Xu, Z., Wang, G., Han, Y., Peng, D., Pang, B., Abbaspour, K.C., Yang, H., 2024. Changes in water conservation and possible causes in the Yellow River Basin of China during the recent four decades. J. Hydrol. 637, 131314. https://doi.org/10.1016/j.jhydrol.2024.131314.

Chiang, Y.-M., Hao, R.-N., Xu, Y.-P., Liu, L., 2022. Multi-source rainfall merging and reservoir inflow forecasting by ensemble technique and artificial intelligence. J. Hydrol. Reg. Stud. 44, 101204. https://doi.org/10.1016/j.ejrh.2022.101204.

Collignan, J., Polcher, J., Bastin, S., Quintana-Segui, P., 2023. Budyko framework based analysis of the effect of climate change on watershed evaporation efficiency and its impact on discharge over Europe. Water Resour. Res. 59, e2023WR034509. https://doi.org/10.1029/2023wr034509.

Dai, A., 2012. Increasing drought under global warming in observations and models. Nat. Clim. Change 3, 52–58. https://doi.org/10.1038/nclimate1633.

Dang, T.H., Coynel, A., Orange, D., Blanc, G., Etcheber, H., Le, L.A., 2010. Long-term monitoring (1960–2008) of the river-sediment transport in the Red River Watershed (Vietnam): Temporal variability and dam-reservoir impact. Sci. Total. Environ. 408, 4654–4664. https://doi.org/10.1016/j.scitotenv.2010.07.007.

Dommenget, D., Latif, M., 2002. A cautionary note on the interpretation of EOFs. J. Clim. 15, 216–225. https://doi.org/10.1175/1520-0442(2002)015<0216:ACNOTI>2.0.CO;2.

Dou, X., Liu, H., Li, M., Zhou, J., Pu, J., Zhai, J., Shen, Y., Peng, Q., Yi, J., 2025. Future evolution characteristics of hydrological drought in the Yuanjiang River Basin under China's dual-carbon scenarios. J. Water Clim. Change 16, 3396–3415. https://doi.org/10.2166/wcc.2025.105.

FAO, 2025. Global Forest Resources Assessment 2025. Food and Agriculture Organization of the United Nations, Rome.

Gao, J., Dai, Z., Mei, X., Ge, Z., Wei, W., Xie, H., Li, S., 2015. Interference of natural and anthropogenic forcings on variations in continental freshwater discharge from the Red River (Vietnam) to sea. Quat. Int. 380-381, 133–142. https://doi.org/10.1016/j.quaint.2015.01.007.

Gleick, P.H., 1986. Methods for evaluating the regional hydrologic impacts of global climatic changes. J. Hydrol. 88, 97–116. https://doi.org/10.1016/0022-1694(86)90199-X.

Gu, Z., Duan, X., Shi, Y., Li, Y., Pan, X., 2018. Spatiotemporal variation in vegetation coverage and its response to climatic factors in the Red River Basin, China. Ecol. Indic. 93, 54–64. https://doi.org/10.1016/j.ecolind.2018.04.033.

Guo, Y., Xu, Y.-P., Xie, J., Chen, H., Si, Y., Liu, J., 2021. A weights combined model for middle and long-term streamflow forecasts and its value to hydropower maximization. J. Hydrol. 602, 126794. https://doi.org/10.1016/j.jhydrol.2021.126794.

Hamel, P., Guswa, A.J., 2015. Uncertainty analysis of a spatially explicit annual water-balance model: case study of the Cape Fear basin, North Carolina. Hydrol. Earth Syst. Sci. 19, 839–853. https://doi.org/10.5194/hess-19-839-2015.

Holland, J.H., 1975. Adaptation in natural and artificial systems. University of Michigan Press, Ann Arbor.

Hua, D., Mo, X., Hu, S., Song, X., 2025. Evolutionary mechanisms of water conservation services in the Yarlung Zangbo River. J. Hydrol. Reg. Stud. 58, 102197. https://doi.org/10.1016/j.ejrh.2025.102197.

IPCC, 2023. Climate Change 2023: Synthesis Report. Contribution of Working Groups I, II and III to the Sixth Assessment Report of the Intergovernmental Panel on Climate Change. IPCC, Geneva. https://doi.org/10.59327/ipcc/ar6-9789291691647.

Jozaghi, A., Shen, H., Ghazvinian, M., Seo, D.-J., Zhang, Y., Welles, E., Reed, S., 2021. Multi-model streamflow prediction using conditional bias-penalized multiple linear regression. Stoch. Environ. Res. Risk Assess. 35, 2355–2373. https://doi.org/10.1007/s00477-021-02048-3.

Lai, X., Chen, H., Hou, Y., Finlayson, B., Li, M., Chen, J., 2021. Lowering water level of Dongting lake of the Mid-Yangtze River in response to large-scale dam construction: A 60-year analysis. Geomorphology 391, 107894. https://doi.org/10.1016/j.geomorph.2021.107894.

Lange, S., 2019. Trend-preserving bias adjustment and statistical downscaling with ISIMIP3BASD (v1.0). Geosci. Model. Dev. 12, 3055–3070. https://doi.org/10.5194/gmd-12-3055-2019.

Le, T.P.Q., Garnier, J., Billen, G., Théry, S., Chau, V.M., 2007. The changing flow regime and sediment load of the Red River, Viet Nam. J. Hydrol. 334, 199–214. https://doi.org/10.1016/j.jhydrol.2006.10.020.

Leng, J., Ma, K., Gu, S., Zhang, K., He, D., 2024. A non-stationary impactquant framework for assessing the human activity impacts on hydrological drought in the Upper Red River. Atmos. Res. 304, 107419. https://doi.org/10.1016/j.atmosres.2024.107419.

Li, M., Di, Z., Yao, Y., Ma, Q., 2024. Variations in water conservation function and attributions in the Three-River Source Region of the Qinghai–Tibet Plateau based on the SWAT model. Agric. For. Meteorol. 349, 109956. https://doi.org/10.1016/j.agrformet.2024.109956.

Liang, X., Lettenmaier, D.P., Wood, E.F., Burges, S.J., 1994. A simple hydrologically based model of land surface water and energy fluxes for general circulation models. J. Geophys. Res. Atmos. 99, 14415–14428. https://doi.org/10.1029/94JD00483.

Liang, X., Wood, E.F., Lettenmaier, D.P., 1996. Surface soil moisture parameterization of the VIC-2L model: Evaluation and modification. Glob. Planet. Change 13, 195–206. https://doi.org/10.1016/0921-8181(95)00046-1.

Liaqat, M.U., Casanueva, A., Ansari, R., Grossi, G., Ranzi, R., 2025. Energy balance modelling of snow and ice melt for the Naltar catchment (Karakoram, Pakistan) in future climate. J. Hydrol. 649, 132411. https://doi.org/10.1016/j.jhydrol.2024.132411.

Liu, C., He, D., Wang, H., Zhong, R., Duan, X., Deng, B., Zhang, E., Li, Y., 2025. Water yield service in the Lancang-Mekong River Basin: Cross-border changes and driving factors. Ecol. Indic. 176, 113725. https://doi.org/10.1016/j.ecolind.2025.113725.

Maraun, D., Wetterhall, F., Ireson, A.M., Chandler, R.E., Kendon, E.J., Widmann, M., Brienen, S., Rust, H.W., Sauter, T., Themeßl, M., 2010. Precipitation downscaling under climate change: Recent developments to bridge the gap between dynamical models and the end user. Rev. Geophys. 48, RG3003. https://doi.org/10.1029/2009RG000314.

Maraun, D., Widmann, M., 2018. Cross-validation of bias-corrected climate simulations is misleading. Hydrol. Earth Syst. Sci. 22, 4867–4873. https://doi.org/10.5194/hess-22-4867-2018.

Menapace, A., Dhawan, P., Dalla Torre, D., Kaffas, K., Crespi, A., Larcher, M., Righetti, M., Cannon, A.J., 2025. Review of bias correction methods for climate model outputs in hydrology. J. Hydrol. 660, 133213. https://doi.org/10.1016/j.jhydrol.2025.133213.

Miralles, D.G., Bonte, O., Koppa, A., Baez-Villanueva, O.M., Tronquo, E., Zhong, F., Beck, H.E., Hulsman, P., Dorigo, W., Verhoest, N.E.C., Haghdoost, S., 2025. GLEAM4: global land evaporation and soil moisture dataset at 0.1° resolution from 1980 to near present. Sci. Data 12, 416. https://doi.org/10.1038/s41597-025-04610-y.

Montanari, A., Nguyen, H., Rubinetti, S., Ceola, S., Galelli, S., Rubino, A., Zanchettin, D., 2023. Why the 2022 Po River drought is the worst in the past two centuries. Sci. Adv. 9, eadg8304. https://doi.org/10.1126/sciadv.adg8304.
Moriasi, D.N., Arnold, J.G., Van Liew, M.W., Bingner, R.L., Harmel, R.D., Veith, T.L., 2007. Model evaluation guidelines for systematic quantification of accuracy in watershed simulations. Trans. ASABE 50, 885–900. https://doi.org/10.13031/2013.23153.
Ngo, L.L., Madsen, H., Rosbjerg, D., 2007. Simulation and optimisation modelling approach for operation of the Hoa Binh reservoir, Vietnam. J. Hydrol. 336, 269–281. https://doi.org/10.1016/j.jhydrol.2007.01.003.
Nguyen, H.H., Nguyen, D.L., Tran, T.V.N., Bui, T.H., Ung, T.T.H., Bui, D.D., Vu, D.L., Hossain, F., Lee, H., 2018. Hydrological model using ground- and satellite-based data for river flow simulation towards supporting water resource management in the Red River Basin, Vietnam. J. Environ. Manag. 217, 346–355. https://doi.org/10.1016/j.jenvman.2018.03.100.
Nguyen, H.Q., Ho, H.L., Park, E., 2023a. Characterizing sediment load variability in the Red River system using empirical orthogonal function analysis: Implications for water resources management in data poor regions. J. Hydrol. 624, 129891. https://doi.org/10.1016/j.jhydrol.2023.129891.
Nguyen, H.Q., Tran, Q.V., Ha, N.T., Nguyen, T.D.H., 2024. Long-term water level dynamics in the Red River basin in response to anthropogenic activities and climate change. Sci. Total. Environ. 912, 168985. https://doi.org/10.1016/j.scitotenv.2023.168985.
Nguyen, T.H., Nguyen, H.Y., Balistrocchi, M., Peli, M., Vu, M.C., Ranzi, R., 2023b. Salinity dynamics under different water management plans coupled with sea level rise scenarios in the Red River Delta, Vietnam. J. Hydro-Environ. Res. 51, 67–81. https://doi.org/10.1016/j.jher.2023.10.003.
Nijssen, B., O'Donnell, G.M., Lettenmaier, D.P., Lohmann, D., Wood, E.F., 2001a. Predicting the discharge of global rivers. J. Clim. 14, 3307–3323. https://doi.org/10.1175/1520-0442(2001)014<3307:PTDOGR>2.0.CO;2.
Nijssen, B., Schnur, R., Lettenmaier, D.P., 2001b. Global retrospective estimation of soil moisture using the variable infiltration capacity land surface model, 1980–93. J. Clim. 14, 1790–1808. https://doi.org/10.1175/1520-0442(2001)014<1790:GREOSM>2.0.CO;2.
O'Connell, E., 2017. Towards adaptation of water resource systems to climatic and socio-economic change. Water Resour. Manag. 31, 2965–2984. https://doi.org/10.1007/s11269-017-1734-2.
Raftery, A.E., Gneiting, T., Balabdaoui, F., Polakowski, M., 2005. Using Bayesian model averaging to calibrate forecast ensembles. Mon. Weather. Rev. 133, 1155–1174. https://doi.org/10.1175/MWR2906.1.
Ranzi, R., Colosio, P., Galeati, G., 2024. Climatology of snow depth and water equivalent measurements in the Italian Alps (1967–2020). Hydrol. Earth Syst. Sci. 28, 2555–2578. https://doi.org/10.5194/hess-28-2555-2024.
Ranzi, R., Eccel, E., Colosio, P., Michailidi, E.M., 2025. A multi-century meteo-hydrological analysis in the Italian Alps: Daily streamflow (1862–2022) at different time scales. Hydrol. Process. 39, e70305. https://doi.org/10.1002/hyp.70305.
Ranzi, R., Le, T.H., Rulli, M.C., 2012. A RUSLE approach to model suspended sediment load in the Lo river (Vietnam): Effects of reservoirs and land use changes. J. Hydrol. 422-423, 17–29. https://doi.org/10.1016/j.jhydrol.2011.12.009.
Šatalová, B., Kenderessy, P., 2017. Assessment of water retention function as tool to improve integrated watershed management (case study of Poprad river basin, Slovakia). Sci. Total. Environ. 599-600, 1082–1089. https://doi.org/10.1016/j.scitotenv.2017.04.227.
Shamseldin, A.Y., O'Connor, K.M., Liang, G., 1997. Methods for combining the outputs of different rainfall–runoff models. J. Hydrol. 197, 203–229. https://doi.org/10.1016/S0022-1694(96)03259-3.
Sharma, P., Mondal, A., 2022. Probabilistic Budyko-based separation of climate and catchment effects on streamflow. J. Hydrol. 608, 127665. https://doi.org/10.1016/j.jhydrol.2022.127665.
She, Y., Chen, J., Zhou, Q., Wang, L., Duan, K., Wang, R., Qu, S., Xu, M., Zhao, Y., 2024. Evaluating losses from water scarcity and benefits of water conservation measures to intercity supply chains in China. Environ. Sci. Technol. 58, 1119–1130. https://doi.org/10.1021/acs.est.3c07491.
Sun, L., Lan, Y., 2020. Statistical downscaling of daily temperature and precipitation over China using deep learning neural models: Localization and comparison with other methods. Int. J. Climatol. 41, 1128–1147. https://doi.org/10.1002/joc.6769.
Teutschbein, C., Seibert, J., 2012. Bias correction of regional climate model simulations for hydrological climate-change impact studies: Review and evaluation of different methods. J. Hydrol. 456-457, 12–29. https://doi.org/10.1016/j.jhydrol.2012.05.052.
Trædal, L.T., Angelsen, A., 2020. Policies drive sub-national forest transitions in Vietnam. Forests 11, 1038. https://doi.org/10.3390/f11101038.
Trenberth, K.E., Dai, A., van der Schrier, G., Jones, P.D., Barichivich, J., Briffa, K.R., Sheffield, J., 2013. Global warming and changes in drought. Nat. Clim. Change 4, 17–22. https://doi.org/10.1038/nclimate2067.
Vigerstol, K.L., Aukema, J.E., 2011. A comparison of tools for modeling freshwater ecosystem services. J. Environ. Manag. 92, 2403–2409. https://doi.org/10.1016/j.jenvman.2011.06.040.
Viney, N.R., Bormann, H., Breuer, L., Bronstert, A., Croke, B., Frede, H., Gräff, T., Hubrechts, L., Huisman, J., Jakeman, A., 2009. Assessing the impact of land use change on hydrology by ensemble modelling (LUCHEM) II: Ensemble combinations and predictions. Adv. Water Resour. 32, 147–158. https://doi.org/10.1016/j.advwatres.2008.05.006.
Wang, H.M., Chen, J., Xu, C.Y., Zhang, J., Chen, H., 2020. A framework to quantify the uncertainty contribution of GCMs over multiple sources in hydrological impacts of climate change. Earth'S. Future 8, e2020EF001602. https://doi.org/10.1029/2020ef001602.
Wang, L., Zhang, F., Shi, X., Zeng, C., Xiang, Y., Wang, Y., 2025. Assessment of meteorological, agricultural and hydrological droughts in Central Himalaya region under climate change. J. Hydrol. Reg. Stud. 60, 102586. https://doi.org/10.1016/j.ejrh.2025.102586.
Wang, R., Li, L., Gentine, P., Zhang, Y., Chen, J., Chen, X., Chen, L., Ning, L., Yuan, L., Lü, G., 2022. Recent increase in the observation-derived land evapotranspiration due to global warming. Environ. Res. Lett. 17, 024020. https://doi.org/10.1088/1748-9326/ac4291.
Wang, S., Zhang, B., Wang, S., Xie, G.-D., 2021. Dynamic changes in water conservation in the Beijing–Tianjin Sandstorm Source Control Project Area: A case study of Xilin Gol League in China. J. Clean. Prod. 293, 126054. https://doi.org/10.1016/j.jclepro.2021.126054.
Woo, S., Kim, W., Chang, S.W., Chung, I.-M., 2025. Seasonal hydrologic responses to climate change based on a CMIP6 multi-model ensemble: A case study of An-Seong watershed in South Korea. J. Hydrol. Reg. Stud. 60, 102491. https://doi.org/10.1016/j.ejrh.2025.102491.
Wu, Q., Song, J., Sun, H., Huang, P., Jing, K., Xu, W., Wang, H., Liang, D., 2023. Spatiotemporal variations of water conservation function based on EOF analysis at multi time scales under different ecosystems of Heihe River Basin. J. Environ. Manag. 325, 116532. https://doi.org/10.1016/j.jenvman.2022.116532.
Xiao, F., Wang, X., Fu, C., 2023. Impacts of land use/land cover and climate change on hydrological cycle in the Xiaoxingkai Lake Basin. J. Hydrol. Reg. Stud. 47, 101422. https://doi.org/10.1016/j.ejrh.2023.101422.
Xu, D., Sun, R., Duan, Q., Liang, Z., Wang, X., Ma, Y., 2026. Integrated multi-dimensional framework for water conservation capacity evaluation and attribution in the Yellow River water conservation area. J. Hydrol. 668, 134979. https://doi.org/10.1016/j.jhydrol.2026.134979.
Xu, M., Xu, G., Liu, S., Li, J., Li, Z., Cheng, Y., Zhuang, J., Dang, Y., Wang, B., Gu, F., 2025. Changes in water conservation and a new estimation for its future potential. Catena 250, 108761. https://doi.org/10.1016/j.catena.2025.108761.
Yin, L., Tao, F., Zhai, R., Chen, Y., Hu, J., Wang, Z., Fu, B., 2022. Impacts of future climate change and atmospheric CO_2 concentration on ecosystem water retention service. Earth'S. Future 10, e2021EF002138. https://doi.org/10.1029/2021ef002138.
Zhai, R., Tao, F., 2021. Climate change in China affects runoff and terrestrial ecosystem water retention more than changes in leaf area index and land use/cover over the period 1982–2015. J. Geophys. Res. Biogeosci. 126, e2020JG005902. https://doi.org/10.1029/2020jg005902.
Zhai, R., Tao, F., Xu, Z., 2018. Spatial–temporal changes in runoff and terrestrial ecosystem water retention under 1.5 and 2 °C warming scenarios across China. Earth Syst. Dyn. 9, 717–738. https://doi.org/10.5194/esd-9-717-2018.
Zhang, G., Wu, Y., Li, H., Yin, X., Chervan, A., Liu, S., Qiu, L., Zhao, F., Sun, P., Wang, W., Jin, Z., 2024a. Assessment framework of water conservation based on analytical modeling of ecohydrological processes. J. Hydrol. 630, 130646. https://doi.org/10.1016/j.jhydrol.2024.130646.

Zhang, K., Chen, H., Ma, N., Shang, S., Wang, Y., Xu, Q., Zhu, G., 2024b. A global dataset of terrestrial evapotranspiration and soil moisture dynamics from 1982 to 2020. Sci. Data 11, 445. https://doi.org/10.1038/s41597-024-03271-7.

Zhang, Y., Mao, J., Zhang, Y., Zhou, B., Qiu, Z., Dong, Y., Zhong, R., 2025. Spatiotemporal dynamics and transboundary differences in fractional vegetation cover in the Red River Basin from 2000 to 2023. Remote. Sens. 17, 2986. https://doi.org/10.3390/rs17172986.

Zhao, G., Tian, S., Liang, S., Jing, Y., Chen, R., Wang, W., Han, B., 2024. Dynamic evolution trend and driving mechanisms of water conservation in the Yellow River Basin, China. Sci. Rep. 14, 26304. https://doi.org/10.1038/s41598-024-78241-5.